JGR Atmospheres

RESEARCH ARTICLE
10.1029/2020JD033414

This article is a companion to Fritts et al. (2020), https://doi.org/10.1029/2020JD033412.

Key Points:
- High-spatial resolution observations captured the breakdown of a Kelvin-Helmholtz instability (KHI) in the mesosphere
- Observations reveal strong interactions among adjacent KHI billows via the formation of vortex tubes and knots
- KHI billow interactions and their rapid cascade to turbulence were initiated by atmospheric gravity wave perturbations of the shear layer

Supporting Information:
- Supporting Information S1
- Movie S1
- Movie S2
- Movie S3

Correspondence to:
J. H. Hecht,
james.hecht@aero.org

Citation:
Hecht, J. H., Fritts, D. C., Gelinas, L. J., Rudy, R. J., Walterscheid, R. L., & Liu, A. Z. (2021). Kelvin-Helmholtz billow interactions and instabilities in the mesosphere over the Andes Lidar Observatory: 1. Observations. *Journal of Geophysical Research: Atmospheres*, *126*, e2020JD033414. https://doi.org/10.1029/2020JD033414

Received 29 JUN 2020
Accepted 2 NOV 2020
Accepted article online 9 NOV 2020

Kelvin-Helmholtz Billow Interactions and Instabilities in the Mesosphere Over the Andes Lidar Observatory: 1. Observations

J. H. Hecht[1], D. C. Fritts[2], L. J. Gelinas[1], R. J. Rudy[1], R. L. Walterscheid[1,3], and A. Z. Liu[3]

[1]Space Science Applications Laboratory, The Aerospace Corporation, El Segundo, CA, USA, [2]GATS, Boulder, CO, USA, [3]Department of Physical Sciences, College of Arts and Sciences, Embry-Riddle Aeronautical University, Daytona Beach, FL, USA

Abstract A very high spatial resolution (~25 m pixel at 90 km altitude) OH airglow imager was installed at the Andes Lidar Observatory on Cerro Pachón, Chile, in February 2016. This instrument was collocated with a Na wind-temperature lidar. On 1 March 2016, the lidar data showed that the atmosphere was dynamically unstable before 0100 UT and thus conducive to the formation of Kelvin-Helmholtz instabilities (KHIs). The imager revealed the presence of a KHI and an apparent atmospheric gravity wave (AGW) propagating approximately perpendicular to the plane of primary KHI motions. The AGW appears to have induced modulations of the shear layer leading to misalignments of the emerging KHI billows. These enabled strong KHI billow interactions, as they achieved large amplitudes and a rapid transition to turbulence thereafter. The interactions manifested themselves as vortex tube and knot features that were earlier identified in laboratory studies, as discussed in Thorpe (1987, https://doi.org/10.1029/JC092iC05p05231; 2002, https://doi.org/10.1002/qj.200212858307) and inferred to be widespread in the atmosphere based on features seen in tropospheric clouds but which have never been identified in previous upper atmospheric observations. This study presents the first high-resolution airglow imaging observation of these KHI interaction dynamics that drive rapid transitions to turbulence and suggest the potential importance of these dynamics in the mesosphere and at other altitudes. A companion paper (Fritts et al., 2020, https://doi.org/10.1029/2020JD033412) modeling these dynamics confirms that the vortex tubes and knots yield more rapid and significantly enhanced turbulence relative to the internal instabilities of individual KHI billows.

1. Introduction

Despite its importance throughout the atmosphere and in other fluids, a quantitative understanding of turbulence and its generation has eluded scientists for many years (Eames & Flor, 2011). While turbulence theory has advanced greatly since the 1941 work of Kolmogorov translated in Kolmogorov et al. (1991), and idealized geophysical sources are now well known (Fritts et al., 2017; Nappo, 2013; Thorpe, 1987, 2005), the character and evolutions of instabilities accounting for laminar to turbulent flow transitions in more general geophysical flows are diverse and largely without significant quantitative observational guidance.

Much of the guidance, related to Kelvin-Helmholtz instabilities (KHIs) arising due to unstable shears, is based on the pioneering laboratory experiments performed by and discussed in Thorpe (1985, 1987, 2002). Thorpe used tilting fluid chambers to simulate the production and evolution of fluid instabilities such as KHIs. Photographs of the fluid evolution revealed primary and secondary KHI structures as well as other turbulent-like features. However, the necessity of fixed boundaries and a limited range of fluid properties and initial flow conditions in such studies seemed, heretofore, to restrict the interpretation of these data when applied to the Earth's atmosphere.

Perhaps surprisingly, new measurement capabilities in the upper mesosphere and lower thermosphere (MLT) offer one of the best opportunities to explore the character and diversity of these important dynamics that occur in many geophysical fluids. Specifically, the ability to combine high-resolution imaging of MLT layers with multi-instrument definition of the underlying larger-scale flows and atmospheric gravity waves (AGWs) offers the potential to quantify these diverse dynamics better in the MLT than at any other altitude region in the atmosphere, or in any other geophysical fluid of which we are aware. This is because large AGW

scales and the viscous MLT enable instabilities, such as KHIs, which can be easily observed with some MLT imaging systems. Fortunately, the decay of these instabilities into turbulence also occurs on horizontal spatial scales that can be resolved by some ground-based airglow and polar mesospheric cloud (PMC) imaging systems. A number of studies using *these* imaging techniques have investigated KHI turbulence dynamics (Baumgarten & Fritts, 2014; Fritts et al., 1993, 2014, 2017; Hecht, 2004; Hecht et al., 2005, 2014, 2018).

The ability of airglow imaging to see small vertical scale features is due to the fact that the airglow layer, at approximately 7 to 10 km vertical width (Hecht et al., 2005), is much thicker than the instabilities. These instabilities, sometimes referred to as ripples when seen in airglow images, typically have vertical extents around 1 km comparable to the vertical extent of the shear layer (e.g., Hecht et al., 2005). The relative scale sizes of the airglow layer and the instabilities allow the entire instability/turbulence layer to be seen in airglow imaging, since, unlike AGWs, the instability features do not suffer from systematic phase cancelation effects (Liu & Swenson, 2003; Swenson & Liu, 1998). These small-scale instability features can perturb the background airglow emission by a few percent (Hecht et al., 2005). Their contrast can be enhanced by differencing two successive images to remove much of the background airglow emission. PMC imaging also has the ability to see very small features, even finer (below 20 m pixel resolution) than the best current airglow imaging. PMC imaging is hampered, though, by the thickness of the brightest portion of the PMC, often a km thick or less (Fritts et al., 2020), that lessens the chance of PMC imaging revealing the entire vertical extent of the instability.

The full potential of imaging is only realized, though, when those data are combined with other techniques that can provide details on the vertical structure of the instability dynamics. Examples of these techniques that have been used to study KHI dynamics include the innovative use of radars (Chau et al., 2020; Hysell et al., 2012; Lehmacher et al., 2007), chemical releases from sounding rockets (Larsen et al., 2005; Mesquita et al., 2020), and lidars used in several of the studies cited above.

Multi-instrument ground-based observatories, such as the Andes Lidar Observatory (ALO) (30.25°S, 70.73°W, 2,530 m) at Cerro Pachón in northern Chile, which houses imagers and a lidar, are ideal for detailed studies of both upper mesosphere mountain waves and more general AGWs, and of KHIs and other large-scale instabilities. Such joint imaging/lidar studies can follow the decay of features that eventually result in turbulence. Previous ALO studies of AGW and instability breakdown into turbulence combined (1) OH airglow imaging data obtained by the Aerospace Nightglow Imager (ANI), at ~500 m pixel resolution, (2) height-resolved wind and temperature data from the University of Illinois at Urbana-Champaign (UIUC) Na lidar data, and (3) direct numerical simulations (DNS) of idealized flows to aid interpretations of instability evolutions. Several investigations using ALO data have revealed generally good agreement between the data and the modeling on the spatial and temporal scales of the observed instability breakdown processes, and they revealed some important features driving turbulence generation, such as horseshoe-shaped vortex rings (Fritts et al., 2014; Hecht et al., 2005, 2014, 2018). These studies also suggested that an effective turbulent viscosity, ν_{turb}, can be estimated in cases where secondary instability scales driving the transition to turbulence depend on the Reynolds number, *Re*.

A comparison of these works suggests the need for somewhat better spatial resolution. Hecht et al. (2005) studied KHI breakdown at Maui. They showed that while the KHI lifetimes were generally in agreement with models, the image data suggested that secondary convective instabilities did not form as expected and that the event's Reynold number was quite low, perhaps even below 300. Little obvious turbulence was apparent in the images. At ALO however, Hecht et al. (2014) did see the expected secondary instabilities and the accompanying turbulence. The Reynolds number was estimated to be about 2,500 based on modeling by Fritts et al. (2014). However, the 500 m pixel size limited observations of scale sizes to features bigger than 1 km, precluding observations of smaller-scale turbulence. While the focus in Hecht et al. (2018) was on mountain wave breakdown, KHIs were also seen. The KHI data also suggested a Reynolds number above 1,000. The main feature of this study was the appearance of horseshoe-shaped vortex rings which are expected to be a feature of gravity wave breakdown but not to appear in KHI breakdown. It is thus expected, as has been the case in other fields, that observations at new scales might reveal the discovery of new features.

In early 2016, an advanced airglow camera, the Aerospace Nightglow Imager 2 (ANI2), allowing high-spatial resolution (~22–27 m at 89 km altitude) of the same OH emission was installed as a replacement for the ANI. ANI2 images have the potential to reveal unprecedented views of instability evolutions, especially with the

use of processing techniques such as image differencing, by extending observations into the smaller scales of the turbulence inertial range. The interpretation of the images is guided by DNS of the instability evolution.

The motivation for this study was the observation of a spectacular KHI event that occurred during the night of 29 February to 1 March 2016 when both the ANI and ANI2 instruments and the ALO Na wind-temperature lidar were operating. The special nature of this event was fourfold: (1) An AGW was propagating approximately perpendicular to the plane of primary KHI motions (e.g., along the KHI billow cores) and apparently modulated the shear layer causing misaligned emerging KHI billow axes at several locations. (2) As the KHI billows intensified, these regions exhibited evidence of vortex tubes linking the billow cores where they are misaligned. The vortex tubes interact to form vortex knots. These knots drove rapid KHI breakdown and a cascade to strong turbulence that closely resembled similar events observed in laboratory shear flow studies described by Thorpe (1987, 2002). (3) The event occurred near the peak altitude of the OH airglow emission layer that allowed, via differencing of ANI2 images, an unprecedented and detailed view of the KHI interactions and breakdown to turbulence. (4) We expect that such events may be widespread, given the expectation for frequent AGW modulations of the shear layers enabling KHI formation. This study, and the companion study by Fritts et al. (2020), characterize these new observations in the context of the presence of newly observed MLT features such as vortex tubes and knots and then compare them to the Thorpe laboratory data as well as to the new DNS model results. This study suggests the importance, with respect to turbulence formation, of features in KHI dynamics that had been seen in the laboratory environment and now have been identified in the MLT region.

This paper, which focusses on the observations, is structured as follows. Section 2 describes the ALO instrumentation and analysis methods. The lidar observations and ANI and ANI2 imaging are described in detail in section 3. Section 4 provides a discussion of the ALO observations and a comparison of vortex tube and knot evolutions with those seen in earlier laboratory studies and accompanying modeling in the companion paper by Fritts et al. (2020). A summary of these dynamics and their potential implications is provided in section 5.

2. Experimental Technique

2.1. Instrumentation at the ALO

Observations discussed here were carried out at ALO in north-central Chile. This location yields frequent examples of terrain-generated mountain waves due to a combination of steep terrain, often significant cross-mountain flow, and the frequent occurrence of sustained eastward winds extending into the mesosphere during winter. The extreme dryness of the area, along with the minimal convective activity over Chilean coastal waters to the west, often produce very clear skies, thus allowing excellent nighttime lidar profiling and OH airglow imaging. The waves are generated over a wide range of frequencies, from stationary mountain waves to high frequency waves generated by gusty winds (Walterscheid & Hickey, 2005; Walterscheid, Hickey & Schubert 2013) and/or transient cross-mountain flows. Such waves reaching the mesosphere encounter atmospheric tides that provide variable propagation environments in altitude and time, and the interactions of the waves with the tides can produce strong wind shears (Hecht et al., 2018). These shears predispose the atmosphere to being unstable, and thus the OH airglow emission altitudes (80 to 90 km) might be expected to produce frequent instability events, and these were previously reported as discussed in section 1.

2.1.1. ANI2

The main instrument for this study is The Aerospace Corporation's new near-IR camera that uses the Teledyne model H2RG HgCdTe focal plane array (FPA), which has 2,048 × 2,048 pixels, each with 18 microns on a side. This FPA was originally designed for NASA's James Webb Space Telescope (JWST). For our array, the wavelength cutoff is just above 1.7 microns, and this allows a relatively warm operating temperature for the FPA. Measurements of OH airglow emission signals are possible at temperatures as high as 200 K, but for this study, the temperature, which was sustained by a commercial cryocooler manufactured by Cobham, was always below 140 K.

The ANI2 custom lens provides a 29.6° × 29.6° (47.4 × 47.4 km) field of view (FOV) from edge to edge of the FPA. There is some small distortion between the center and corners of an image. For example, at 89 km distance from the center of the FOV, a representative altitude for this study, the side of the square pixels have a 22.3 m FOV at the center of the field, 24.4 m at the edges of the FOV, and 26.7 m at the corners of the FOV.

We used an astrometric solution, obtained from the numerous stars in the FOV, to determine the offset of the instrument bore-sight (defined to be the line-of-sight of the central pixel of the detector array) from the zenith. This bore-sight is found to be 1.7° west and 2.0° south of zenith, and the entire image is rotated 2.3° clockwise.

For this study, the pixel integration time was 4.55 s. Note that no shutter is used, but the readout electronics read each line sequentially, and based on the available clock speeds, this takes about 1.5 s to read the entire chip. Thus, 1.5 s was the minimum integration time available for this study. The commercial software/electronics board package, however, limited the image cadence to no faster than one image approximately every 20 s. Data were taken during moon down periods, and the camera operated in this mode from February 2016 to September 2018 at ALO. At that time, the cooler failed and ANI2 was returned to Aerospace. A new custom board and software were installed allowing improved image cadence. ANI2 was reinstalled in late January 2020 at ALO.

An additional note should be made of the deficiencies of the ANI2 FPA that is an engineering version of the science-grade Teledyne FPA. The ANI2 FPA has variations in the pixel quantum efficiency and other defects in its electronic structure that affect its operation. With a higher quality scientific H2RG FPA, an image would provide a sky image with minimal evidence of any of the static FPA structure. Any residual static structure could be taken out by flat fielding. For example, these FPAs have 32 individual readout amplifiers, each reading out a 64 pixel wide column. Since there is a small few percent difference in each of these readouts, we did apply a flat field to each image that was derived from the average pixel count for each column. Unfortunately, the ANI2 FPA had some additional pixel-to-pixel non-uniformities that produced an additional background static structure in each image. The extreme variability of the sky emission during the night precluded the generation of a flat field of sufficient quality to remove all of this additional structure. However, this remaining static FPA structure is almost completely eliminated by differencing two images with the same pixel integration time. Hence, as we describe below, we use two differencing techniques that emphasize either the small or large scale atmospheric wave and other atmospheric features in the images. As shown in the movies produced using these techniques, the resultant differenced images showed little or no evidence of any static structure. These difference images are adequate for this study and note that the features seen in the lower resolution ANI images are also seen in the higher resolution ANI2 images.

2.1.2. ANI

The Aerospace Corporation's legacy near-IR camera (ANI) is described in some detail in Hecht et al. (2005) and in Hecht et al. (2014). The camera has a wide-angle lens with a 256 × 256 pixel HgCdTe detector array to provide images over an approximate 73° by 73° region of the sky. In an image, 105 pixels go across the ANI2 FOV with one pixel seeing about 440 m at 89 km altitude. The array consists of four 128 × 128 pixel quadrants, each with their own readout circuitry. A new detector was purchased prior to installation at ALO so that all four quadrants were operational. A fixed open filter position is used allowing a spectral range of 1.55 to 1.7 μm, determined by the internal filters, to be imaged. This spectral range is dominated by the OH Meinel airglow and because the OH Meinel (4,2) band brightness is almost 100 kilo-Rayleighs, the signal to noise ratio (S/N) for a 1 s integration is over 200:1. ANI failed in mid-March 2016 and has not been replaced to date.

In the images for ANI and ANI2, east is at left, and north is at top. For ANI, the lower left quadrant (SE) is quite noisy, and there is a reduced output in portions of the western part of the image. However, the differencing method discussed below removes the latter issue.

2.1.3. Data Reduction for ANI and ANI2

Images are presented in one of two ways that have been discussed in previous publications (Hecht et al., 2005, 2014, 2018). Both methods attempt to increase the contrast of the instabilities and AGWs, both of which tend to have amplitudes of a few percent or less of the background. (1) An image that is the difference of two images taken from 20 to 70 s apart. This method is used for both the ANI and ANI2 images. The reason this is effective is as follows: The background AGWs nominally travel at 50 m/s or less and have horizontal wavelengths typically between approximately 20 to 45 km, for example, Table 1 in Hecht (2004). Thus, in 20 s, the AGW has only advanced 10° to 20° in phase. Image differencing subtracts these two AGWs at only slightly different phases, resulting in an AGW that is greatly reduced in amplitude. For instability features that move with a similar velocity but have much smaller horizontal wavelengths, the differencing of the two images results in much less of a reduction in amplitude. Thus, image differencing tends to eliminate the long wavelength static background, because these features are almost completely eliminated by

the image subtraction, and thus the contrast increases for the smaller scale features, such as KHIs and other smaller-scale instability features. The downside of this approach is that it adds some uncertainty as to the actual structure of the instability features due to their advection by the wind over the difference interval. One other aspect to consider in differencing is that if the difference time is too short, both the AGW and the instabilities will be diminished so much in amplitude that the features will have weak contrast and be hard to see. This is especially true if the pixel size is large. So, for ANI where the pixel size is around 500 m, a 60 s difference actually results in better contrast than a 20 s difference.

(2) An alternative approach, which is used for the ANI2 processing, is to choose one image (where the background structure is close to uniform) and subtract that from all other images. This technique was used in the study of mountain waves by Hecht et al. (2018). The instability features are not differenced and thus some of the uncertainty of the first method is reduced. However, the longer wavelength background is not completely eliminated, and thus the contrast is not as good as in Method (1).

A comparison between the ANI and ANI2 images is presented later in the discussion of the resultant movies. Both sets of images though see the same large scale structure.

2.1.4. Smearing and Small-Scale Features in the ANI2 Images

The scale sizes that are associated with turbulence are often bounded by the smaller scale of turbulence that is typically less, and often much less, than 1 km in the altitude region near 90 km, which is of importance to this study (e.g., Roper & Brosnahan, 1997). The ANI2 pixel size at the main altitude of interest for this study, 89 km, is between 22 and 27 m, and the integration time is 4.55 s for each pixel. For this study, data are presented binned either 2×2 or 4×4, resulting in an effective pixel size of around 50 or 100 m, with some variation depending on the distance from the center of the FPA. ANI2 images, shown later, reveal many small-scale features that are associated with the breakdown of KHIs. However, associating these features quantitatively with turbulence is hampered by the following uncertainty. The ANI2 integration time coupled with the background winds results in a smearing of between 150 to 250 m in the direction of the wind motion. Thus, the small-scale features that are advected with the wind may appear somewhat elongated along the wind direction. However, it is important to note that the full native ANI2 resolution is retained in the direction perpendicular to the wind direction, and thus the scale-sizes of structures can be measured. Nevertheless, even though the small-scale structures could be characterized as turbulence if their separations are a few hundred meters or less, their elongation does complicate some comparisons with model simulations. Hence, these features will simply be referred to as chaotic, small-scale features.

It is important to note that the smearing does not affect, in any meaningful way, features such as KHIs or AGWs that have scales much larger than 500 m. The effect of smearing also does not affect measurements of the wavelengths of the secondary convective instabilities, whose structures are aligned almost along the wind vector. In that case, the wavelength measurements are perpendicular to the wind motion and therefore retain the full native ANI2 resolution. Finally, the smearing issue should be less in future studies where the integration times are less, typically around 3 s.

2.1.5. University of Illinois at Urbana-Champaign/Embry-Riddle Aeronautical University Lidar

The University of Illinois at Urbana-Champaign/Embry-Riddle Aeronautical University (UIUC/ERAU) Na Lidar provides vertical profiles of wind, temperature and Na density at high vertical (500 m) and temporal (1 min) resolutions. The two horizontal components of the wind vector were calculated from the line of sight (LOS) wind measured when the lidar beam was pointed to 20° off-zenith toward the south (S) or the east (E). The vertical component is the LOS wind when the lidar beam was pointed to zenith (Z). The beam was pointed to these three directions in the sequence ZEZS with 1 min dwell time in each direction. The horizontal wind was derived from the off-zenith LOS wind as described in Liu et al. (2002). They were then smoothed with a 15-min full-width Hamming window in time at every 6 min and 500 m interval. Note that the east and south winds fall outside the FOV of ANI2.

At 6 min and 500 m intervals, the line-of-sight (LOS) wind and temperature errors are about 6 m/s and 1 K, respectively, in the 88 to 89 altitude range of interest to this study. These errors are larger at 85 km and below and at 95 km and above. The errors of temperature and wind are dominated by photon noise and were calculated based on the well-established error analysis described in Gardner and Papen (1995) and in Gardner (2004). Although these errors appear small, some of the derived quantities depend on spatial derivatives and thus are very sensitive to small changes in the temperature and wind altitude profiles. Therefore, to reduce the error in the derived quantities while still maintaining the necessary resolution, the lidar data

have had an additional 3-point smoothing applied in the vertical direction, and the derived shear directions had a final 3-point smoothing in the temporal direction. This instrument has been used in previous work (Hecht et al., 2014) that investigated the decay of KHIs into turbulence.

The lidar data are mainly used to determine the stability of the atmosphere with respect to the formation of a KHI. The stability of atmospheric regions is most easily quantified by the Richardson number, Ri, (Richardson & Shaw, 1920) which is given by

$$\mathrm{Ri} = \frac{N^2}{(dU/dz)^2}, \tag{1a}$$

or

$$\mathrm{Ri} = \frac{(g/T)(dT/dz + g/C_p)}{(dU/dz)^2}, \tag{1b}$$

where N is the Brunt-Vaisälä (BV) frequency and dU/dz is the horizontal wind shear, the variation of U, the horizontal wind velocity, as a function of z, the altitude (Hecht et al., 2018). The square of N is given by the numerator of Equation 1b where T is the temperature, dT/dz is the vertical temperature gradient, g is the magnitude of the gravitational acceleration (Deng et al., 2008; Hirt et al., 2013), taken as 9.5 m/s^2 to adjust for altitude, and C_p is the atmospheric specific heat at constant pressure. The quantity g/C_p is the adiabatic lapse rate, which is about 9.5 K/km in the 85 to 90 km altitude region, and the vertical temperature gradient is the negative of the atmospheric lapse rate. Thus, N^2 depends on the difference between the adiabatic lapse and the measured atmospheric lapse rate.

As noted in the extended discussion of instability formation in Hecht et al. (2018) and earlier in Fritts et al. (2014), when Ri is below 0.25 conditions become favorable for the formation of KHIs, though instabilities can and do form at larger values due to parametric instabilities (e.g., Walterscheid et al., 2013).

2.1.6. AGW Wavenumber Using Lidar and Imager Data

The analysis of AGW intrinsic parameters follows from the dispersion relations shown below (e.g., Hecht, 2004). Consider an AGW at an altitude z above the ground in an atmosphere where H is the pressure scale height. The vertical wavenumber, m, is given by $2\pi/\lambda_z$, where λ_z is the vertical wavelength. The vertical wavenumber obeys the following dispersion relation derived assuming a WKB approximation under the assumption of a slowly varying m over a vertical wave cycle (Einaudi & Hines, 1970; Fritts & Alexander, 2003; Hecht, 2004)

$$m^2 = (2\pi/\lambda_z)^2 = \frac{(N^2 - \omega_I^2)(k^2 + l^2)}{(\omega_I^2 - f^2)} + \frac{\omega_I^2}{c_s^2} - \frac{1}{4H^2}, \tag{2a}$$

$$m^2 = \frac{(N^2 - \omega_I^2)(k^2 + l^2)}{(\omega_I^2 - f^2)} + \frac{(\omega_I^2 - \omega_a^2)}{c_s^2}. \tag{2b}$$

In Equation 2a, c_s is the speed of sound, ω_I is the intrinsic frequency, which is the frequency measured in the frame of reference that moves with the background wind, and f is the inertial frequency which is $2\Omega\sin(\phi)$, where ϕ is latitude and Ω is the angular speed of the Earth. Also, k and l are the vector components of the horizontal wavenumber, k_h, whose magnitude, $(k^2 + l^2)^{0.5}$, is equal to $2\pi/\lambda_h$. For a given background wind velocity component, $\overline{U}$, in the direction of k_h, and an observed wave horizontal phase velocity, c_o, the intrinsic wave phase velocity, c_I is given by c_o-$\overline{U}$ which is equal to ω_I/k_h. The observed (ground-based) period, τ_g, is equal to λ_h divided by c_o. The intrinsic period, τ_I, is equal to λ_h divided by c_I. In Equation 2b, the acoustic cutoff frequency, ω_a, is given by $c_s/(2H)$ in an isothermal atmosphere. When m^2 is negative, the AGW is evanescent and it is not freely propagating vertically. Such a region can form a boundary for a trapped or ducted AGW. Note that for most AGWs observed in the airglow layer, the last term of Equations 2a or 2b is of minor importance.

3. Data for 0000 to 0320 UT on 1 March 2016

ANI (ANI2) data are available from just before (after) 0000 (00 hr 00 min) UT to about 0300 UT on 1 March 2016. The main focus of this paper is on the spectacular KHI event that enters the FOV of ANI about 0020

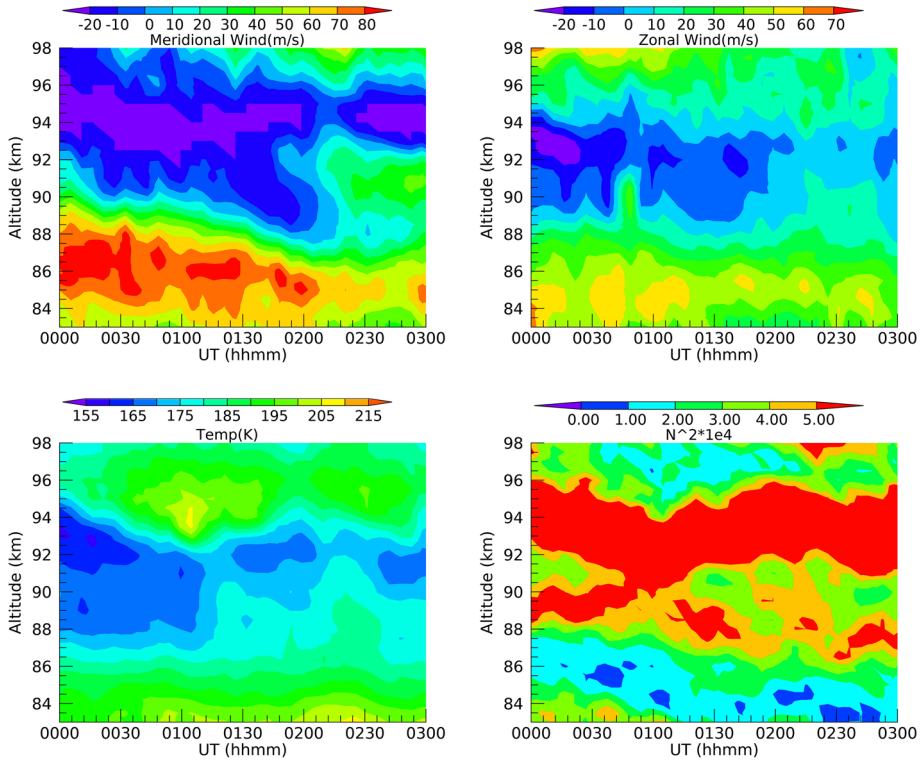

Figure 1. Four-panel plots of the derived measurements from the lidar data as functions of time and altitude where time is hhmm UT on 1 March 2016. Upper left, meridional wind. Upper right, zonal wind. Lower left, T at 5° intervals. For clarity, the colorbar only shows labels every 10°. Lower right, N^2 times 1×10^4 in s^{-2}.

UT and shows chaotic features until about 0120 UT. The core of this event occurs from about 0020 UT to 0050 UT. Data after the core period constrains the duration of the event. Later data also reveal a second KHI event that is not a focus of this work.

Three movies are included in the supporting information as supplemental documents. Movie S1 presents the ANI difference images, Movie S2 presents the ANI2 difference images using differencing technique 1, and Movie S3 presents the ANI2 difference images using differencing technique 2. Note again that the first differencing technique subtracts two images taken 1 min or less apart, while the second technique always subtracts a fixed image.

3.1. Background State Derived From ALO Lidar Data

Figures 1–3 show the background state of the atmosphere versus time after 0000 UT. Figure 1 has four panels that show the meridional and zonal winds, the temperature, and the derived values for N^2 as a function of altitude from 83 to 98 km. For the period before ~0050 UT, N^2 was at or below its nominal value (around 4×10^{-4} s^{-2}) in the altitude region below 89 km. This was the region where KHI formation could be favored.

Figure 2 shows the magnitude and direction of the wind and the wind shear, the gradient of the horizontal wind in the vertical. Negative gradients in temperature occur between 85 and 89 km while large wind shears occur between 87 and 91 km before 0050 UT (hhmm UT). The overlap between these two regions is between 87 and 89 km, altitudes where there would be the most favorable conditions for KHI formation. Thus, it can be seen that the most favorable location for KHI formation at altitudes below 90 km altitude and at times before 0140 UT is likely between 0030 to 0040 UT, and around 87 to 89 km. The other two panels of Figure 2 show the wind and shear directions that can be compared to the imager observations shown later in this study. Note that because the alignment of an instability in the airglow images is ambiguous to a 180° reflection, the shear directions are mapped into a 0 to 180° regime by subtracting 180° if the direction is above 180°. The downward progression in altitude, from about 90 to 86 km, of both the shear magnitude and direction suggests a tidal influence.

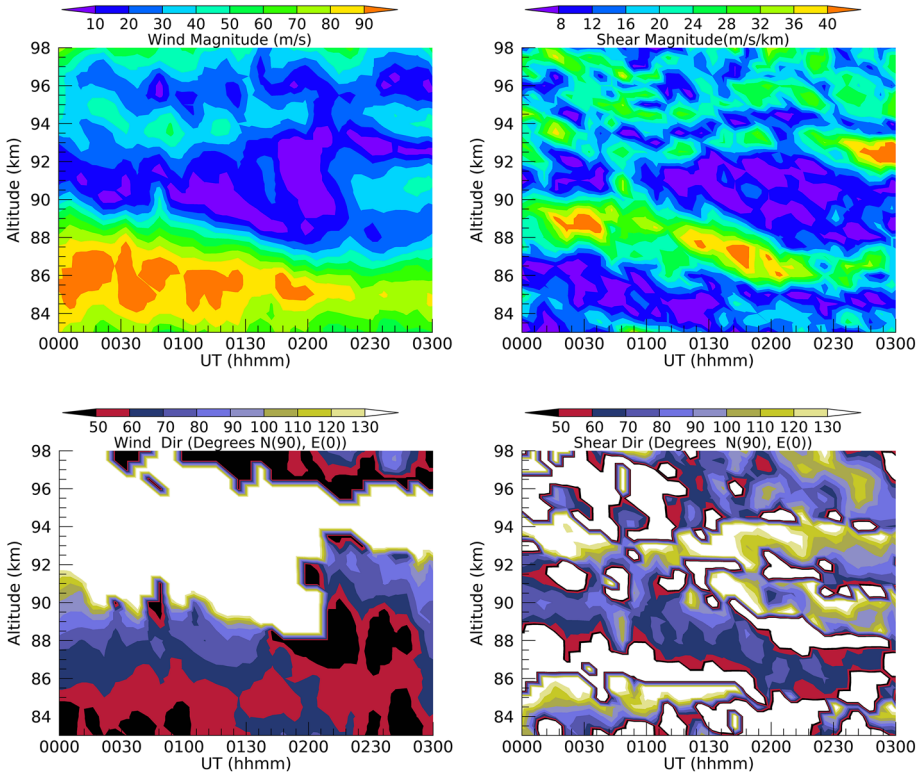

Figure 2. Same as Figure 1 but for the following lidar-derived quantities. Upper left, wind magnitude. Upper right, shear magnitude. Lower left, wind direction with north at 90° and east at 0°. Lower right, shear direction with the same convention.

The optimal formation region for KHI is quantified by Ri shown in Figure 3. The upper left and right panels show Ri versus time with upper limits of the color scale occurring at either 0.25 or 0.30. Values of Ri above that value are uncolored. These two values are chosen because an Ri value below 0.25 classically suggests an instability region suitable for KHI formation. Thus, the upper left panel only shows colored regions when Ri is at or below that value. This allows the reader to easily see where KHI formation is likely to occur. However, we recognize the uncertain nature of the measurement. Hence, we show in the upper right panel with an Ri of 0.3 as a maximum that shows colored values for regions at or below that value. This, along with the other two panels on the bottom, allows the reader to assess the uncertainty in such a measurement.

The other two panels of Figure 3 show the effect of considering a one-sigma uncertainty in Ri. Considering the uncertainties in the data, these panels show that below 90 km and before 0100 UT, the most favorable region for KHI formation should be near 88 to 89 km at around 0030 to 0040 UT. At later times, another favorable region occurs between 0200 and 0220 UT, around 84 to 86 km altitude. The lower right panel provides some insight into the uncertainty in Ri at the time (0030 to 0040 UT) and at the altitude region (around 89 km) where KHI formation could occur.

We also note that there are additional uncertainties in the these lidar-derived Ri values that use wind measurements from off-zenith observations. Because the lidar measurements are not taken precisely where the KHIs are seen, background waves can cause local perturbations which can modify the temperature and wind gradients, potentially significantly lowering Ri. This will be discussed further in section 4.

The wind data in Figure 2 should allow a determination of where the instability formation is occurring. Around 0030 UT at 86 km, the wind is high, ~80 to 100 m/s, while at 89 km, it is much lower, ~40 to 50 m/s. The peak shear, before 0100 UT is around 40 m/s/km at 89 km at around 0030 UT. Since KHIs advect with the wind the imager data allow the instability speed to be determined, and when these data are compared to the measured wind the KHI altitude can be determined.

Finally, we note that there are additional data on the state of the atmosphere on this night. Level 2A SABER (Sounding of the Atmosphere using Broadband Emission Radiometry) data on the NASA TIMED satellite

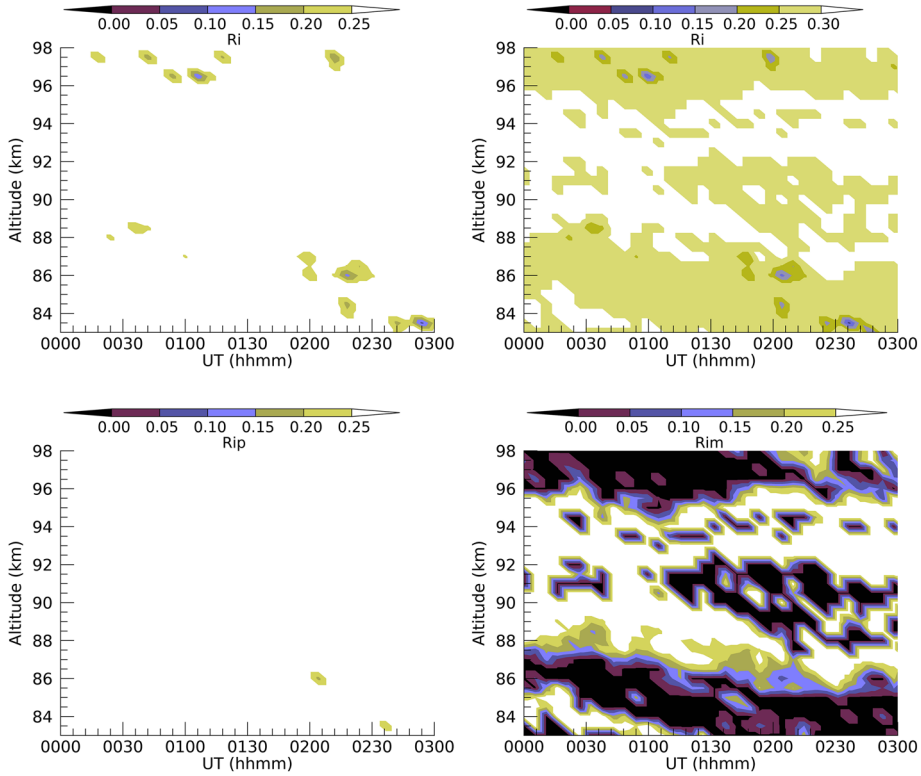

Figure 3. Four-panel plots of lidar-derived Ri versus time and altitude as noted in Figure 1. Upper left, Ri. Upper right, Ri showing an expanded scale above 0.25. Lower left, Ri plus one sigma error. Lower right, Ri minus one sigma error.

publicly available at http://saber.gats-inc.com show that the nighttime OH Meinel 1.6 μm emission seen over ALO peaked near 88 km. Thus, for the main event period before 0100 UT, where Ri was near or below 0.25 at 89 km altitude, the observed instabilities are originating at or near the peak of the OH emission layer.

3.2. Overview of the Image Data

These movies show the passage of AGWs through a region of developing KHI, and the resulting interactions and evolutions of KHI vortex tubes and knot dynamics that are the subjects of this paper and the companion paper by Fritts et al. (2020). The movies and images extracted from the movies, both discussed below, provide the context for our discussion of the image sequences.

The ANI image shown in Figure 4 is a difference image of two images taken 60 s apart with the first image initiated at 003536 UT (0 hr 35 min 36 s UT). As noted above, the lower left quadrant is noisy, but waves are still visible. The white/black pairs are stars that move from left to right (east to west) during the 60 s difference period. The large-scale wavelike features whose phasefronts are aligned roughly from the NE to SW corners are AGWs that are propagating generally toward the NW. The wavelike features nearly perpendicular to the AGWs are KHI billows that are advecting toward the NE. The red box, rotated clockwise by about 4°, is the approximate field of view of the ANI2 imager. The ANI2 FOV is also rotated clockwise by about 4°, and thus the rotation shows the uncertainty of the absolute ANI and ANI2 alignments and FOVs.

Note that although the nominal pixel size is ~25 m or less in the original ANI2 images, in these figures, the pixels are all binned 4 × 4 to produce 512 pixel by 512 pixel images. The original, full resolution data have been examined and for the purposes of this study ~100 m pixel size (4 × 4 binning) appears to be sufficient to resolve most features of interest visually, although 2 × 2 binning (50 m pixel size) does reveal some finer scale features. The 2 × 2 binning is used for some of the line plots in Figures 10 and 11.

Figure 5 shows two ANI2 difference images produced via the techniques described in section 2.1.3. Panel a, on top, is a 23 s difference image between images with exposures initiated at 003511 and at 003534 UT. The exposure time for each is 4.55 s. As noted earlier, there is some smearing of structures along their direction of motion. Panel b, on the bottom, is an image at 003511 UT with with frame 72 at 000953 UT subtracted

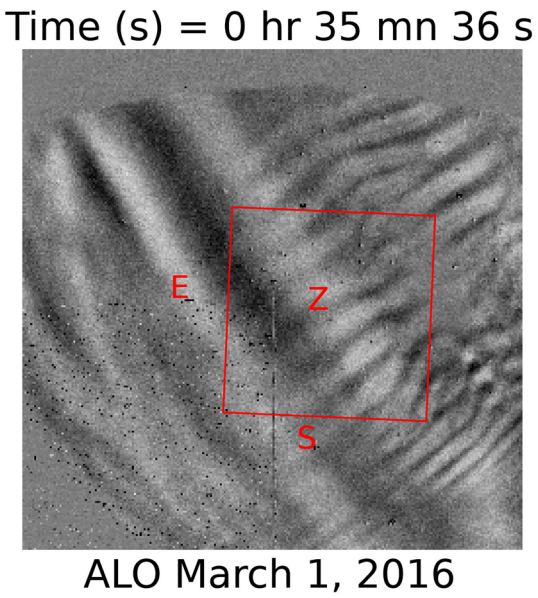

Figure 4. ANI image initiated at 003536 UT (hhmmss UT). The lidar pierce points are shown as the zenith (Z), 20° south (S) of Z, and 20° east (E) of Z. The red box is the approximate FOV of ANI2.

using the second method of differencing, described in section 2.1.3. Panel a shows a number of key features that will be described below. For reference to Panel a, Panel b shows the same white line 1 from the SE to NW corner. This white line can be used to guide the eye to follow the AGW peak in both Panel a, where the AGWs are suppressed, and in Panel b where the peaks are prominent. A quantitative use of all the white lines is presented later in section 4.1.1. Note that except for Movie S3, all the other images are of the first and more traditional differencing technique.

Of interest here is the comparison of the features between these two differencing techniques. Note that in Panel a, the regions where the AGW peaks in intensity (the whitest pixel regions) are displaced from the same peak regions in Panel b. The reason for the peak displacement seen in Panel a is because that method emphasizes the regions with the steepest brightest gradients, whereas the second method shows the actual regions of peak emission. The significance of this will be discussed in a later in section 4.2.1. Also, while the general features shown in Panel a can be discerned in Panel b, the lower contrast of Panel b, due to the presence of the full brightness AGWs, makes it difficult to see the detail shown in Panel a.

When viewing the movies and the first technique difference images shown in Figures 7–9, discussed below, note the following summary of the key physical processes highlighted in the top panel of Figure 5.

1. AGWs are roughly propagating from the lower left (SE) corner to the upper right (NW) corner. The red arrow, marked A, designates the distance between two AGW phasefronts which here is about 26 km. White line 1 is from corner to corner and is slightly rotated from the actual AGW direction of motion. This line is also repeated in the bottom panel.
2. KHIs are generally advecting from the lower right (SW) corner to the upper left (NE) corner, almost perpendicular to their phasefronts. The KHIs phasefronts are roughly perpendicular to the AGW phasefronts. The dark green arrow, marked B, designates the distance between two KHI phasefronts, which here is about 10 km. The peaks in white line 2 are used to determine that distance.
3. KHI phasefronts advect with the horizontal wind (along white line 2) and are at around 89 km altitude based on the horizontal wind velocity as measured by the lidar.
4. The KHI phasefronts are essentially perpendicular to the shear directions measured by the lidar near 89 km. Note that based on Figure 2 the wind and shear directions are both close to 70°. The convention we use is the same as for Figure 2 where north is at 90° and east is at 0°.
5. The AGW modulation of the large-scale shear layer, specifically the shear thickness and shear magnitude, yields regions at the KHI formation stage that initiate KHI billows having different wavelengths and growth rates.
6. As the KHI billows approach large amplitudes, manifested in the images as having higher contrast, they also extend along their axes, sometimes causing misaligned, noticeably curved, ends between adjacent initial regions of strong KHI growth.
7. Intensifying shears between these misaligned billows induce vortex tubes (orange lines in Figure 5) to form on the vortex sheets between the misaligned billow cores. As these vortex tubes are advected, they become entwined with an adjacent billow/vortex tube leading to an "X" pattern (knot region). The blue arrow, marked C, points to such an X pattern, also highlighted in blue. The discussion section expands on this somewhat based on the model presented in Fritts et al. (2020). Note that smaller vortex tubes are present that can also connect billows. One such vortex tube is highlighted by the orange arrow, marked D, that connects two billows.
8. The "X" patterns lead to vortex knots as they intensify, appearing as loops or figure eights (Fritts et al., 2020), where two billow cores at both sides of a misalignment lead to dramatically accelerated transitions to stronger turbulence. This is shown in the sequence of images presented in Figures 7–9.
9. Other instabilities, especially convective instabilities within individual KHI billows, arise that are aligned roughly orthogonal to the KHI billows, but these arise more slowly and lead to weaker turbulence compared to the knot region. Their separation can be used to estimate *Re* of the event following

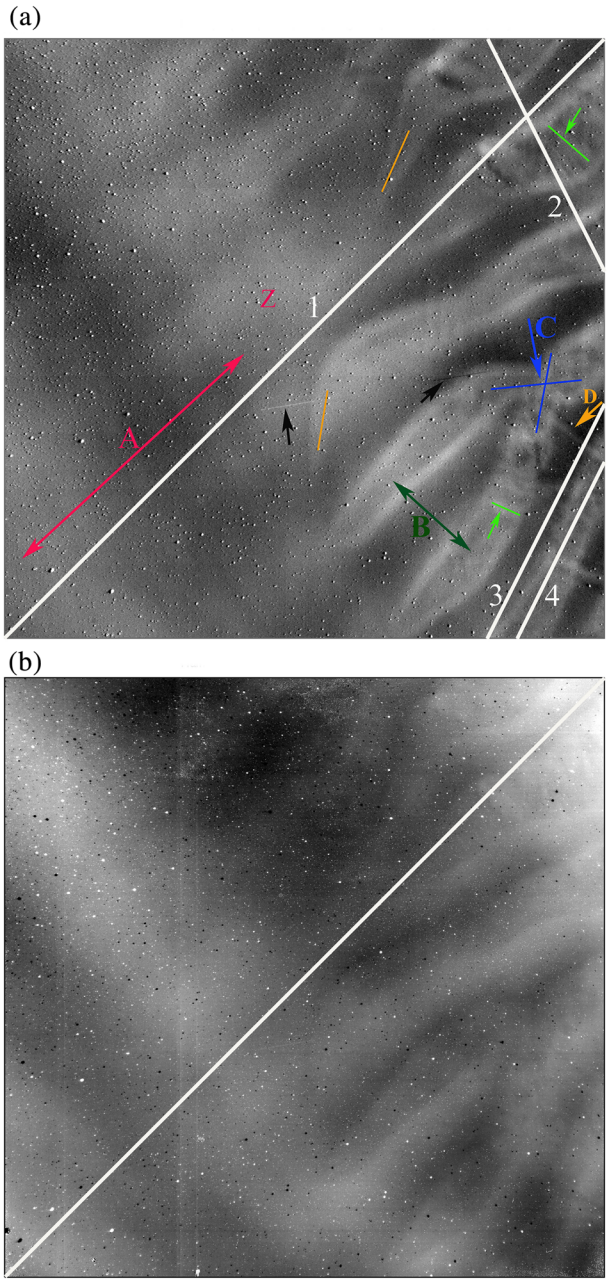

Figure 5. (a) Difference between two images exposed for 4.55 s at 003511 and at 003534 UT. These difference images are in Movie S2. This image is labeled as follows with more information in the text. White line 1(2) allows the AGW(KHI) wavelength to be determined. The cross-sections of these lines are shown in Figure 10. White lines 3(4) allow structures outside(inside) the KHI billow to be measured. The cross-sections of these lines are shown in Figure 11. Red double-headed Arrow A points to two AGW peaks. Dark green double-headed Arrow B points to two KHI billows. Blue Arrow C points to a blue "X" indicating the main knot region. Orange Arrow D points to a thin vortex tube connecting two KHI billows. The two unmarked orange lines indicate growing vortex tubes that will connect billows. The unmarked light green arrows span two KHI billows. The black line points to a meteor trail. (b) The image at 003534 UT with frame 72 at 000953 UT subtracted. Similar difference images are in Movie S3. The same white line as white line 1 in the top panel is shown for reference.

earlier work discussed in Hecht et al. (2018). A convective roll is highlighted by the light green arrow pointing to a light green line.

10. The counts along the lines 3 and 4 will be plotted later in Figure 11 to provide a quantitative measure of the convective instability or vortex tube scales.
11. The short black arrows point to meteor trails that are often seen in ANI2 images.

3.3. ANI Movie S1

Movie S1 is a nominally 60 s difference movie that starts just before 0000 UT on 1 March 2016 and ends just before 0330 UT. In each frame, a red box outlines the approximate field of view (FOV) of the ANI2 imager. Since the nominal pixel size is about 500 m, this movie gives a good view of the wave and instability features in the over 100 km square FOV surrounding the ANI2 FOV. This movie provides quantitative information on the scale size and motions of the KHIs and the larger-scale AGWs. These are summarized next. Note that the times refer to times shown in the movie.

1. AGWs with horizontal wavelengths over the entire night between 20 and 40 km are propagating from the SE to NW throughout the entire night. If we take 0° to be an eastward motion (toward the left) and positive north (clockwise), the AGW motion is ~155° at the beginning of the observation period and ~140° at the end. This motion is roughly 70° from the wind direction, as shown in Figure 2, which is toward 80° at the beginning of the observation period, shifting to below 70° after 0200 at 89 km altitude. The observed period of the AGWs is about 11 min, which gives a nominal velocity of ~40 m/s for a 26 km wavelength. The intrinsic period is still above 300 s, the nominal BV period, for these observations.
2. Bright irregular bands that are presumably KHIs are first seen entering from the lower right quadrant (SW) around 0020 UT, just about the time the lidar data suggest that the atmosphere becomes unstable. These features enter the ANI2 red square region around 0025 UT. The horizontal wavelengths are between 8 and 12 km with shorter wavelengths being more representative of the earlier KHIs. The KHI billows quickly become distorted and misaligned, with a knot first being seen to begin to form around 0028 UT just before entering the ANI2 region. The distorted billow cores first decay into chaotic small-scale features around 0034 UT, and by 0105 UT the ANI2 region seems to be nearly free of such features and KHIs. The modulation of the KHIs by the AGWs traveling at right angles seems to have contributed to local enhanced KHI growth and misalignment of billow cores thereafter. It is clear, however, that many of the features are below the resolution of the ANI.
3. Another set of KHIs appears outside the ANI2 region after 0205 UT, corresponding to an unstable atmosphere at a later time based on the Ri data in Figure 3.
4. Based on an observed AGW period of 11 min and a horizontal wavelength of 26 km, Figure 6 shows a plot of m^2 versus time and altitude, where m^2 is calculated using the lidar measurements of the wind and temperature profiles. It does appear that a partial wave duct could exist with a freely propagating region from about 87 to 95 km, and with possible regions where m^2 could be below zero outside this region. Such a duct would explain the almost constant observations of waves as they would have been produced elsewhere and ducted overhead.

3.4. ANI2 Movie S2

Movie S2 is a nominally 23 s difference movie that starts just after 0000 UT on 1 March 2016 and ends just before 0230 UT. As in the ANI movie the black and white moving dots are stars moving from east to west (north is at the top).

The significance of this movie is its ability to resolve the features, highlighted in Figure 5, thus providing a more detailed time history of their evolutions. For example, the knot region is first seen entering from the lower right corner at 003039 UT in frame 186-184. This decays into chaotic, small-scale features by frame 234-232, about 9 min later. Other knots also form during this period, and this will be discussed in somewhat more detail below. By frame 254-252 at 004330 UT, the NW portion of the image shows chaotic, small-scale features, while the SE portion shows four to five KHIs that have not evolved secondary convective instabilities. These break down by frame 282-280, around 5 min later. Over the next 25 min, these apparently turbulent flows dissipate and are advected outside the FOV. One aspect of this dissipation is the apparent production of features that resemble vortex rings such as were observed in Hecht et al. (2018). As noted in section 1, these features are not associated with KHI breakdown. These are apparent in the movie around 0050 UT. A few comments on these features will be made later.

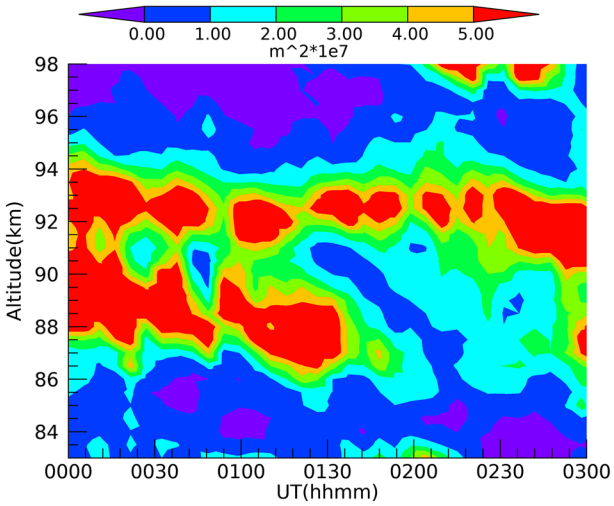

Figure 6. Single-panel plot of lidar data-derived m^2 versus time and altitude following Figure 1.

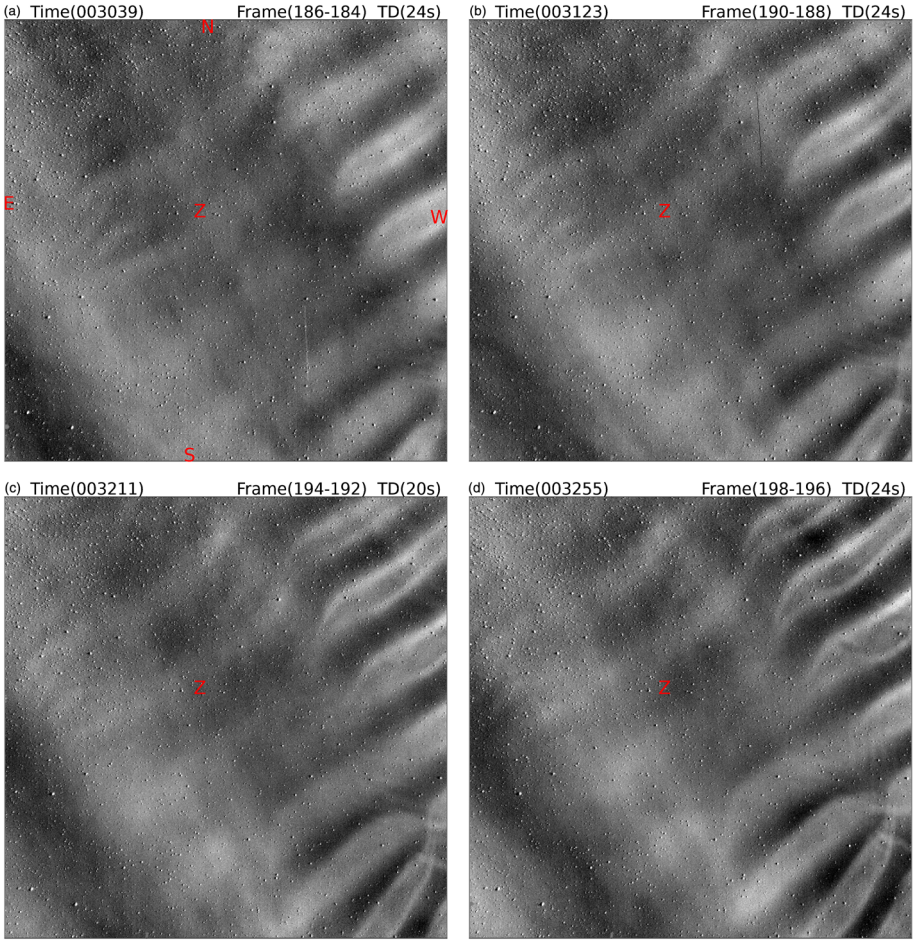

Figure 7. Four-panel difference images of ANI2 data. All the panels are binned to 512 by 512 pixels. The frame numbers, the time difference between the two images (TD), and the beginning UT in (hhmm) are given in the header. Panel (a) starts at 003039 UT. Panel (b) starts at 003123 UT. Panel (c) starts at 003211 UT. Panel (d) starts at 003255 UT. The zenith (Z) and four directions, 0° is east (E), 90° is north (N), 180° is west (W), and 270° is south (S). Note that Z is displaced from the central pixel and the image is rotated toward the west by 4°.

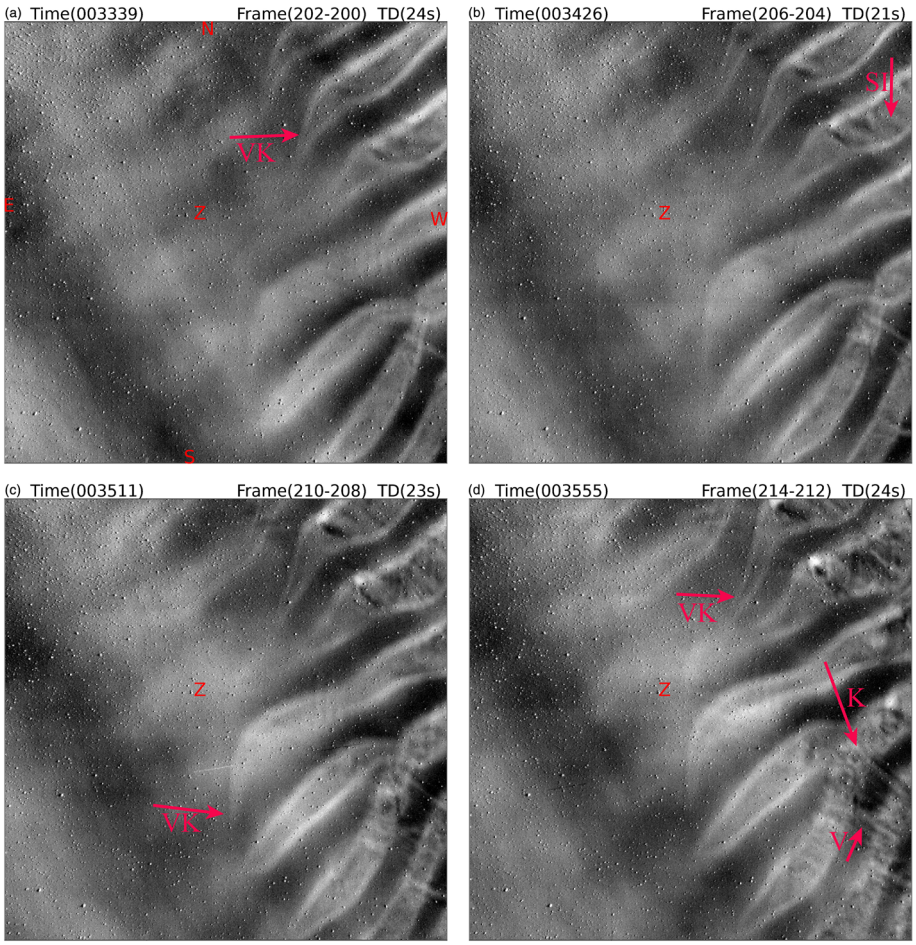

Figure 8. Same as Figure 7 except for the start times. Panel (a) starts at 003339 UT. Panel (b) starts at 003426 UT. Panel (c) starts at 003511 UT. Panel (d) starts at 003555 UT. The arrows point to features that are described in the text.

Subsequent to this, AGWs without any chaotic small-scale features are prominent by frame 482-480 at 0126 UT. Around 0210 UT, as seen in frame 710-708, it appears that features from the second KHI event, seen in the ANI movie, passes through one corner of the FOV.

3.4.1. Details of the Knot Region Observations

It is easier to see and discuss the evolution and decay of the knot region by looking at individual images. Figure 7–9 each have four panels that show the evolution of the knot region from a first appearance in frame 186-184 to a period ~8 min later, shown in frame 230-228. The highlights of this sequence are as follows.

1. In the lower right corner of all the panels of Figure 7, a knot region resembling an X advects into the FOV. However, no chaotic, small-scale features have yet developed in this region. Instead, there appear to be several narrow vortex tubes connecting the billows in the knot region.
2. In Figure 7d, at 003255 UT, note that the KHI whose phasefront is seen in the upper right corner appears to be developing a prominent vortex tube. In the succeeding images, this tube will connect to another KHI billow. The development of this vortex tube is highlighted by arrows in Figures 8 and 9.
3. Figure 8 shows the development of the dynamics as revealed by several interesting features. In Panel a, at 003339 UT, Arrow VK points to the developing vortex tube that will eventually form a knot. Arrow SI in Panel b, at 003426 UT, points the development of secondary convective instabilities. Arrow VK in Panel c, at 003511 UT, points to another large vortex tube extending to connect to another billow and eventually forms a knot. In Panel d, at 003555 UT, Arrow VK points to the connection of two vortex tubes to form a knot. The region around the tip of Arrow K shows some of the chaotic small-scale features that are beginning to form within the knot region. Arrow V points to some possible vortex tubes that are possibly connecting adjacent billows.

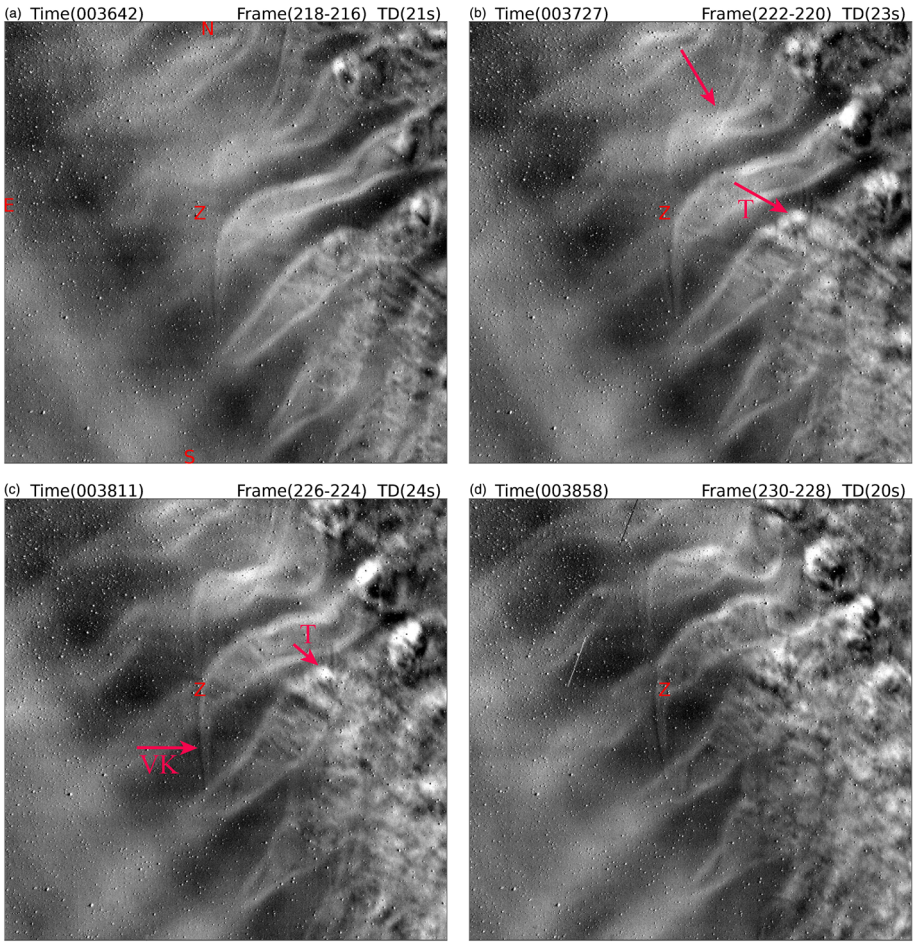

Figure 9. Same as Figure 7 except for the start times and the W direction is not shown. Panel (a) starts at 003642 UT. Panel (b) starts at 003727 UT. Panel (c) starts at 003811 UT. Panel (d) starts at 003858 UT. The arrows point to features that are described in the text.

4. Figure 9 shows the continued development of the dynamics discussed above. In Panel b, at 003727 UT, Arrow K shows the joining of two vortex tube, highlighted in Figures 7 and 8, to form an X pattern knot region. Note that in the subsequent panels, this knot region begins to distort and form considerable chaotic, small-scale features, In Panel c, at 003811 UT, Arrow VK shows the connection of a vortex tube to an adjacent billow, although the knot has not quite formed. Arrow T in Panels b and c points to a possible turbulent feature whose energy dissipation rate is discussed in section 4.1.2.

3.5. ANI2 Movie S3

Movie S3, which shows images with the background removed by subtracting a fixed frame at 000953 UT from all images, is the second of the ANI2 movies and the sequence of images allows one to determine the presence of the wave crests with respect to the KHI decay regions. Note the black dots represent stars in frame 72, which are fixed, while the white dots are stars for each frame and thus these move in the movie. While the passage of the AGW phase fronts does appear to affect the initial growth and misalignment of emerging patches of KHI billows, the decay of the KHIs proceeds even in the absence of this interaction.

4. Discussion

These data are the highest spatial resolution airglow images to date that show the evolution of KHIs. The images and movies show the formation of vortex tubes and knots arising from the interactions of KHI billows and their subsequent breakdown into chaotic smaller-scale features. The sequence of this section is

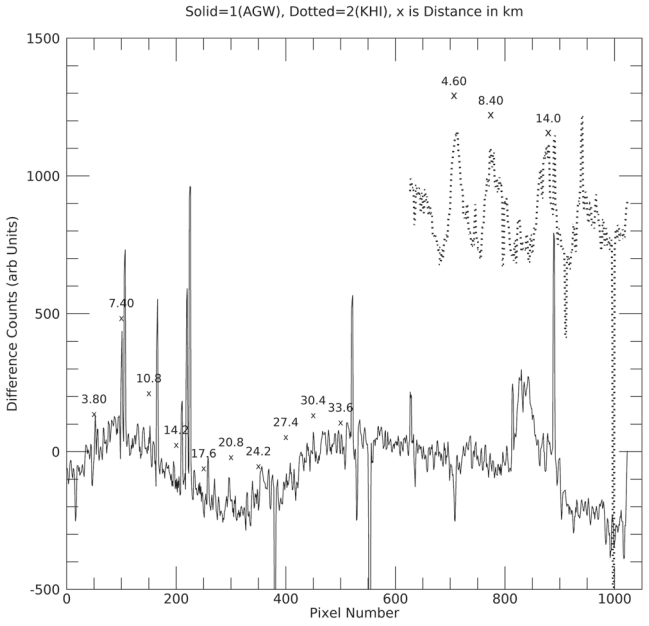

Figure 10. Plot of the difference counts for line 1 (solid) and line 2 (dotted) in Figure 5. These data are from the 2 × 2 binned version of Figure 5a that, as shown, is 4 × 4 binned. The large spikes and dips are stars. The numbers above each line are the distance along the line in km. The distances are calculated using the pixel area appropriate for that pixels position in the lens field imaged at 89 km. For line 1, reference pixel number 0 is the pixel at the lower left corner of the image, in Figure 5a, and distances are measured from that pixel. The reference pixel number is the horizontal pixel number. For line 2, reference pixel number 624 is the pixel at the right edge of Figure 5a, and the distances are measured from that pixel. Here, the reference pixel number represents the vertical pixel number with pixel number 1,023 being at the top edge.

as follows: (1) We first infer the background turbulent viscosity following our previous work (Fritts et al., 2014; Hecht et al., 2014, 2018). (2) Then we use the images to estimate the energy dissipation associated with the decay of the KHI billows following Chau et al. (2020) and Mesquita et al. (2020). (3) Following that, a comparison is made to Thorpe's laboratory data that were the first to reveal KHI tube and knot development. (4) Then a short discussion follows on the possible effects on AGWs on KHI formation in the MLT images and Thorpe's inferences on this same process based on the laboratory simulations. (5) The modeling section will summarize the main points of the associated paper by Fritts et al. (2020) which describe the vortex dynamics driving tube and knot formation, and why the knot regions are so significant. (6) Finally, the results are put into context by a comparison with previous ALO studies.

4.1. Derived Quantities of KHI Dynamics in the MLT

4.1.1. Turbulent Viscosity

Several of our previous studies cited in section 1 used the ratio of the primary to secondary (convective instability) wavelengths to assist in inferring the turbulent viscosity. Figure 10 shows plots of white lines 1 and 2 from Figure 5, although these plots are from the 1,024 × 1,024 image that uses 2 × 2 pixel binning. Such a binned pixel has about 46 m on a side. The solid line in Figure 10 shows the distance across the AGW crests while the dashed line shows the distance across the KHI crests. Also shown above each line is the distance along the line in km. This is calculated incorporating the change in pixel size across the FOV, as discussed in the instrument description section. The AGW peaks occur around pixel numbers 100 and 500, resulting in a distance of about 26 km, even considering the rotation of the phasefront of about 8° from the white line in Figure 5. The uncertainty is around 1 km due to the distortion of the AGW by the underlying KHI.

For line 2 that is used to determine the KHI wavelength, three peaks are shown. The peaks at 4.6 and 8.4 km are the two edges of a single KHI. The peak at 14.0 km is the first peak at the next KHI. Hence, the KHI wavelength is about 9.4 km.

Figure 11 shows plots of the counts along lines 3 and 4 from Figure 5. Line 3 is along the area between two positive phasefronts of a KHI while line 4 is along positive phasefronts. Thus, these lines traverse across the secondary convective instabilities within a phasefront but also include some vortex tubes that may be connecting phasefronts. For line 3, separations are between 1 and 2 km, while line 4 has more well-defined peaks as might be expected since these are likely secondary convective instabilities. For line 4 between the points marked 2 and 14.4, there are eight main peaks. Thus, the average wavelength is 1.77 km and the ratio of the KHI primary to KHI secondary wavelength is 5.3.

Using these data, one can use a modeling analysis (Fritts et al., 2014; Hecht et al., 2014, 2018) to estimate *Re* to be around 1,000, although it could be a little higher if the secondary wavelength is indeed smaller than 1.8 km. Following these same references, the turbulent viscosity ν_{turb} can be derived from $(H_{hw})(U_{hw})/Re$, where H_{hw} is the half-width of the shear layer and U_{hw} is half the shear velocity. If we take λ_{KHI} to be 9.4 km then, following Fritts et al. (2020), H_{hw} is $\sim\lambda_{KHI}/(4\pi)$, which is 750 m. Although the lidar data are smoothed and only have points every 500 m, the measured H_{hw} from the lidar data is about 1 km. This gives some confidence to our derived value. Here, the shear magnitude is taken to be 40 m/s/km, and U_{hw} is calculated by multiplying H_{hw} by 40 m/s/km to be 30 m/s. Hence, ν_{turb} is 22.5 m^2/s at around 89 km, a value close to what was derived in Hecht et al. (2018) at 83 km. This value is an order of magnitude greater than what would be expected in a nominal atmosphere at this altitude (Hecht et al., 2014). Note, though, that if *Re* is somewhat larger, this would reduce the inferred value for ν_{turb}.

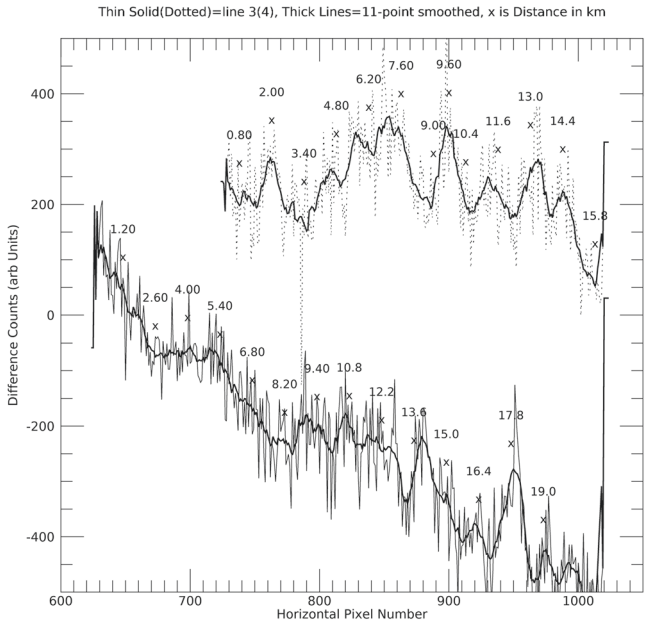

Figure 11. Plot of the difference counts for line 3 (solid) and line 4 (dotted) in Figure 5a. These data are from the 2 × 2 binned version of Figure 5a that, as shown, is 4 × 4 binned. The large spikes and dips are stars. The numbers above each line are the distance along the line in km. The distances are calculated using appropriate pixel area imaged at 89 km. For both lines, the pixel numbers are referenced to horizontal pixels and zero is toward the lower left corner of the image.

4.1.2. Energy Dissipation

Figure 12 shows four panels that illustrate a derivation of the energy dissipation of the feature shown in Figure 9. Here, we derive the wind associated with one of the KHIs that also has a knot region. Panels a and b are aligned by sliding the two original images (Panels b and c of Figure 9) to account for the wind motion. This was done by minimizing the variance in the box and the wind was measured to be 41.7 m/s, a value that places these features near 89 km based on the lidar data, with an estimated uncertainty of 1 m/s. Panel c shows the difference, after this wind motion is accounted for, between Panels a and b. Many residual chaotic features are seen, especially in the knot region. However, the red arrows in Panels a to c isolate one such feature previously shown in Figure 9. This feature is presumably a large feature undergoing motion different from the mean wind that is advecting the KHIs. Panels a and b were displaced an additional amount to minimize the variance of that feature, and the subtraction of those two panels are shown in Panel d. Given the distance moved in the 44 s between these observations, the velocity of this feature is 55.6 m/s. The residual velocity, v_r, after subtracting the mean wind, is 13.9 m/s.

The size of the feature L_e was 1.85 km and thus, following Chau et al. (2020) and Mesquita et al. (2020), an energy dissipation rate, ϵ, was calculated from Cv_r^3/L_e where C is taken to be 1. Using our data, ϵ is 0.97 W/kg. This equation and the constant C are also discussed in earlier work (Chen, 1974; Weinstock, 1981), and it is clear from these references and those in Chau et al. (2020) that there is some uncertainty in this result due to uncertainties in C. In addition, the uncertainty in the horizontal wind produces an additional uncertainty of 20% to 30% on this determination of ϵ. Nevertheless, this value is comparable to that found by Chau et al. (2020) who made measurements at only a slightly lower altitude. Note also that this is a large energy dissipation rate based on Chau et al. (2020). We also point out that the chaotic features that are present in Panels a to c of Figure 12 appear to be near the knot area suggest that the energy dissipation is at least enhanced throughout that region.

We should note, however, that this velocity is not measured in the same way as the two other cited studies. They measured the vertical wind and horizontal and vertical dimensions of the feature, and then they inferred a horizontal root mean square velocity. Mesquita et al. (2020) did follow a KHI crest and their measured root mean square velocity was comparable to what was found for the inferred horizontal wind. In our case, we only have horizontal measurements. We assume that our measured velocity of a feature relative to

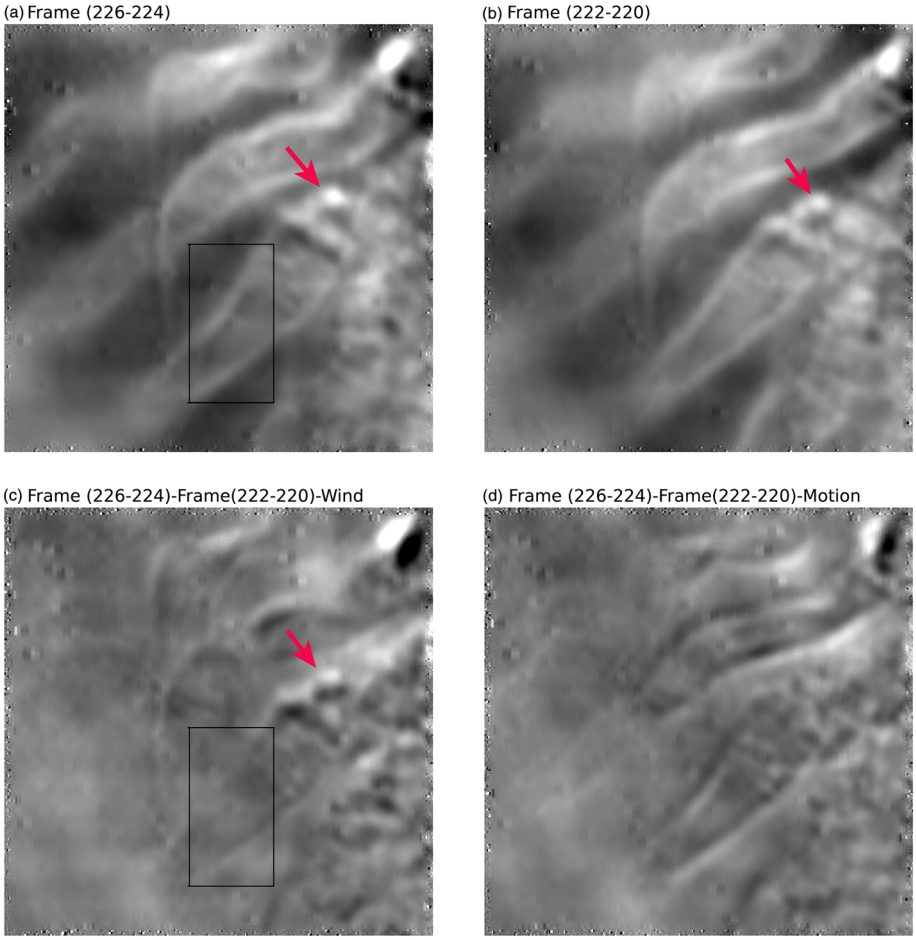

Figure 12. Four panels that illustrate a derivation of the energy dissipation rate of the turbulent feature shown in Figure 9b. These panels first had large spikes due to stars removed. Panel (a) is a portion of Figure 9b, while Panel (b) is a portion of Figure 9c. The rectangle shows the region where the wind was obtained. Panel (c) is the difference of Panels (a) and (b) when they are aligned according to the wind motion. This was done by minimizing the variance in the box, and the wind was 41.7 m/s with an estimated uncertainty of 1 m/s. Panel (d) is the difference when Panels (a) and (b) are aligned to minimize the variance of the selected turbulent feature indicated in Figure 9b.

the mean KHI velocity is comparable to what is inferred from the vertical velocity measurements used in the other studies. We further note that our measured velocity is above the mean wind, and given the wind shear, with decreasing winds at higher altitudes, these features appear to be below the mean altitude of the KHI by about 1/4 of a km.

4.2. Comparison With Laboratory Data

As noted in section 1, Thorpe (1987, 2002) used tilting fluid chambers to reveal the production and evolution of KHIs. Those experiments on KHI evolution showed the development of tubes and knots. In the laboratory data provided in Thorpe (2002), *Re* was around 1,000, comparable to what is found for the present observations, and their laboratory results had a remarkable similarity to what is observed in the atmosphere at 89 km. Figure 13 reproduces a modified version of Figure 2 from Thorpe (2002) that shows the evolution of the knot regions from their initial vortex tubes joining adjacent billows to the development of turbulence. In Panel a of Figure 13, the billow junction of g and h looks quite similar to the knot (X) region highlighted in Figure 5. In Panel b of Figure 12, the laboratory data show several apparent vortex tubes going across billows similar to what is seen in the development of the lower right knot region in Figure 8. The decay of the knot regions into turbulence in the laboratory data, shown in Panels c and d of Figure 13, as well as the distortion of the laboratory KHI billows, resembles the atmospheric data. As an example of the latter, the arrow in Panel d points to emerging very fine scale instabilities within the billow region similar to what is highlighted by the light green arrow in Figure 5. There is a difference though, which will be discussed next.

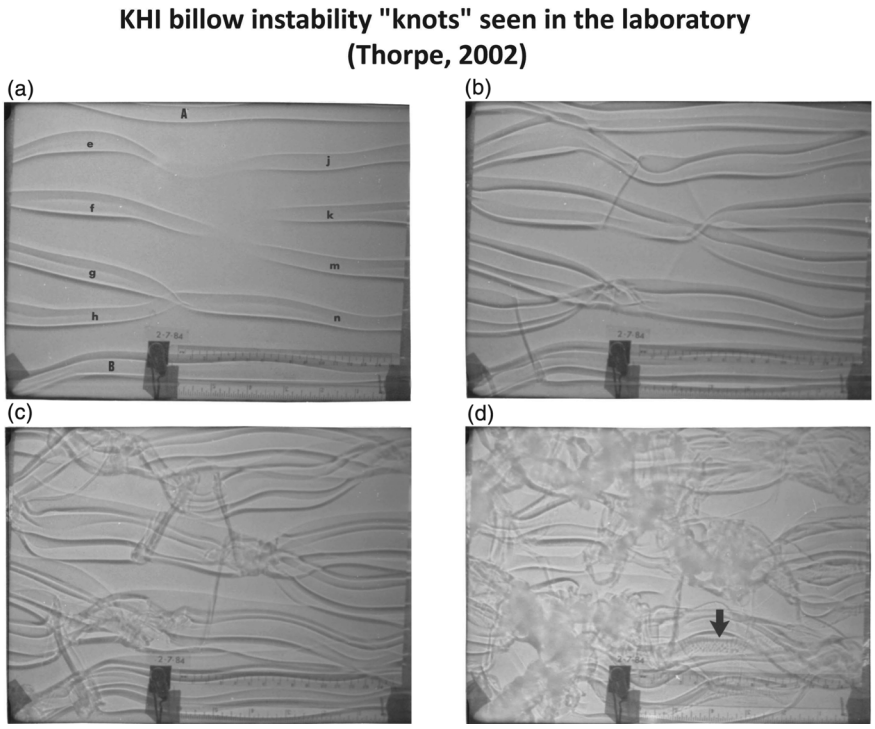

Figure 13. Four-panel images. The panels are based on Figure 2 from Thorpe (2002). The arrow in Panel (d) is from Thorpe (2002) and points to apparent convective rolls in the laboratory data similar to those in the atmosphere indicated by the light green arrow in Figure 5.

4.2.1. AGWs and Knot/Turbulence Formation

In the atmosphere, AGWs can be present that can distort the lifecycle of KHIs. In particular, phases of the AGW can induce an increasing atmospheric lapse rate and wind shear, thereby potentially modifying both N^2 and the wind shear linearly. Thus, since Ri increases linearly with N^2 while decreasing by the square of an increasing wind shear, as portions of the AGW causing vertical compression pass through an atmospheric region, Ri will decrease. This theoretically should either initiate the formation of a KHI as Ri drops below 0.25, or if the KHI is already formed, affect the growth and misalignment of the KHI billows. Note that the steepest gradients of the AGW are displaced 90° from the peak amplitude. The apparent AGW motion of the images differenced by technique 1 (Movie S2), whose observed peaks are displaced from AGW actual peak brightness, may, depending on the phase relationship between brightness and vertical compression, represent a more realistic view of the regions with the lowest Ri values. Indeed, the movies do suggest that the passages of the AGW wave peaks, in Movie S2 are associated with the growth and misalignment of the KHI billows arising in different regions.

Thorpe (2002) specifically discussed knot formation by proposing that the growth rate of the billows could be different due to the presence of AGWs traveling at right angles to the billows, thus resulting in regions where knots could form. Thus, the discussion in Thorpe (2002) anticipated the results found here.

4.3. Multiscale KHI Modeling

The actual processes of knot formation are complex, as evidenced by previous DNS of KHI formation and growth, for example, Fritts et al. (2014). The companion paper by Fritts et al. (2020) performs such a study to determine the nature of knot formation and decay. To simplify the DNS somewhat, knot formation was only considered in the absence of AGWs, although a lower Ri was used that anticipates its reduction in the presence of an AGW. The modeling reported in that study shows clearly, and quantitatively, that turbulence transitions occur much more quickly in the tube and knot regions then in the adjacent, largely undisturbed, KHI billows. But note that the tube and knot dynamics do include the “ends” of KHI billows where they link to mis-aligned billows along their axes.

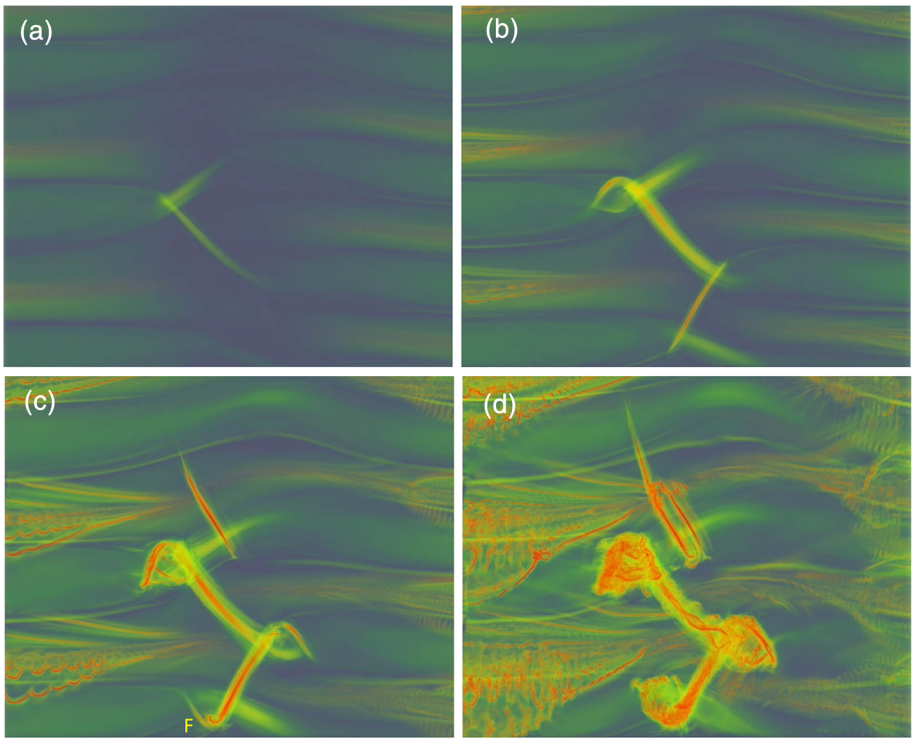

Figure 14. Four panel images, separated by an equal amount of time, based on the results from Fritts et al. (2020).

While the reader is referred to that study for complete details, a few important aspects are shown here in Figure 14. This figure shows four panels, each separated by a uniform spacing in time, that show the development of adjacent, roughly orthogonal vortex tubes to knots and their instability dynamics leading to turbulence. A more detailed description is found in Fritts et al. (2020). One can see the vortex tubes as they interact and join an adjacent billow, a process also seen in the atmospheric data. Of particular note is the confinement of the turbulence to the region of the tubes and knots, as seen the laboratory results. The results of the modeling show that the tube and knot regions accelerate and intensify the generation of turbulence, and these dynamics have never before been addressed by modeling.

4.4. Airglow Observations of the Evolution of KHI Dynamics

As noted in section 1, previous high-spatial resolution airglow observations of KHI breakdown have revealed different lifecycles. At Maui, while the KHI lifetimes (10 to 20 min) were in line with model expectations, secondary instabilities had much larger wavelengths than expected, equal to the KHI primary wavelengths, and little turbulence was observed. *Re* was inferred to be quite low, perhaps below 300 (Hecht et al., 2005). In a previous ALO study (Hecht et al., 2014), secondary instabilities evolved as expected and turbulent structures were quite apparent with analysis of structures down to below 2 km. In this study, *Re* was estimated to be around 2,500. Also at ALO (Hecht et al., 2018), mountain wave breakdown was observed at the same time as KHIs. Vortex-rings were observed as a prominent feature of the wave breakdown. They were not associated with KHI dynamics. The ~500 m pixel size, however, precluded any further quantitative analysis such as the energy dissipation rate, as explored above and in Chau et al. (2020) and Mesquita et al. (2020).

The event described in this study did show secondary convective instability evolution with a primary to secondary wavelength ratio of around 4, consistent with the values seen in the other ALO studies. The *Re* and the turbulent viscosity are not largely different from previous ALO observations. Here though, small-scale chaotic features were, unlike our previous ALO observations, the dominant feature of the KHI evolution during breakdown. This appears to be due the development of the tubes and knots. These features are seen in the laboratory, where waves are not present, and thus are associated with KHI dynamics. The modeling also indicates that tubes and knots can form during KHI breakdown and produce vigorous turbulence. Thus, the combination of these observations of KHI dynamics, the previous laboratory studies of KHIs, and the multiscale modeling of KHI breakdown has advanced our understanding of KHI dynamics.

However, as noted above, after the breakdown of the KHIs are initiated, there is some indication that vortex rings are present. These must be due to the presence of the AGWs. Given the advances that the multiscale modeling has shown when only KHI breakdown is considered, an investigation that includes AGWs would be interesting.

5. Summary

Airglow observations on 1 March 2016 at ALO revealed the presence of bright KHIs advecting with the wind at close to right angles to the motion of AGWs. These interactions occurred in a period when Na lidar observations suggested that the atmosphere was dynamically unstable. The airglow was imaged at two spatial resolutions, and these data revealed the following.

1. These images captured the first direct evidence of specific KHI vortex tube and knot dynamics in the atmosphere, expected based on laboratory studies (Thorpe, 1987, 2002) and suggested to be likely in the atmosphere by Thorpe (2002).
2. While the lower-resolution ANI data were insufficient to identify knot formation in earlier studies and obscure the details of the formation even in this study, the use of the higher resolution ANI2 data and image differencing techniques make the dynamics more apparent, indicating that airglow pixel resolution on the order of 100 m or better is needed to resolve and quantify these phenomena.
3. The knot formation region appears to be a prolific generator of small-scale turbulent-like features. The largest energy dissipation is confined mostly to this region.
4. The energy dissipation rate of about 1 W/kg in the knot region is large, consistent with the discussion found in Chau et al. (2020).
5. Based on the parallel modeling in Fritts et al. (2020), these events are likely to play major roles in the MLT. This is surely also the case at lower altitudes, based on data discussed by Thorpe (2002).
6. In addition, these data support the suggestion by Thorpe (2002) that the growth and misalignment of KHI billows and their formation of knots would be affected by AGWs traveling at right angles to the KHI phasefronts.

Data Availability Statement

The lidar data are available at zenodo.org (https://doi.org/10.5281/zenodo.3911142). The imager data needed for this paper are at zenodo.org (https://doi.org/10.5281/zenodo.4023307).

Acknowledgments
We thank Steve Heathcote and the staff at the Cerro Tololo Inter-American Observatory and especially at SOAR on Cerro Pachón for providing support for all the instrumentation and for the operations at the Andes Lidar Observatory. Support for J. H. H., L. J. G., R. J. R., and R. L. W. was provided by NSF grant numbers AGS1450660 and AGS1911952. The UIUC/ERAU Na lidar operation at ALO was supported by NSF grants AGS-1136278 and AGS-1136208. Support for A. Z. L. was provided by NSF grant AGS-1759471. Support for DCF was provided by grants NSF AGS-1445783 and AGS-1449633, AFOSR FA9550-18-1-0009, and NASA 80NSSC18K0007.

References

Baumgarten, G., & Fritts, D. C. (2014). Quantifying Kelvin-Helmholtz instability dynamics observed in noctilucent clouds: 1. Methods and observations. *Journal of Geophysical Research: Atmospheres*, *119*, 9324–9337. https://doi.org/10.1002/2014JD021832

Chau, J. L., Urco, J. M., Avsarkisov, V., Vierinen, J. P., Latteck, R., Hall, C. M., & Tsutsumi, M. (2020). Four-dimensional quantification of Kelvin-Helmholtz instabilities in the polar summer mesosphere using volumetric radar imaging. *Geophysical Research Letters*, *47*, e2019GL086081. https://doi.org/10.1029/2019GL086081

Chen, W. Y. (1974). Energy dissipation rates of free atmospheric turbulence. *Journal of the Atmospheric Sciences*, *31*(8), 2222–2225. https://doi.org/10.1175/1520-0469(1974)031<2222:EDROFA>2.0.CO;2

Deng, Y., Ridley, A. J., & Wang, W. (2008). Effect of the altitudinal variation of the gravitational acceleration on the thermosphere simulation. *Journal of Geophysical Research*, *113*, A09302. https://doi.org/10.1029/2008JA013081

Eames, I., & Flor, J. B. (2011). New developments in understanding interfacial processes in turbulent flows. *Philosophical Transactions of the Royal Society A: Mathematical, Physical and Engineering Sciences*, *369*(1937), 702–705. https://doi.org/10.1098/rsta.2010.0332

Einaudi, F., & Hines, C. (1970). WKB approximation in application to acoustic-gravity waves. *Canadian Journal of Physics*, *48*, 1458–1471. https://doi.org/10.1139/p70-185

Fritts, D. C., & Alexander, M. J. (2003). Gravity wave dynamics and effects in the middle atmosphere. *Reviews of Geophysics*, *41*, 1003. https://doi.org/10.1029/2001RG000106

Fritts, D. C., Isler, J. R., Thomas, G. E., & Andreassen, O. (1993). Wave breaking signatures in noctilucent clouds. *Geophysical Research Letters*, *20*(19), 2039–2042. https://doi.org/10.1029/93GL01982

Fritts, D. C., Kaifler, N., Kaifler, B., Geach, C., Kjellstrand, C. B., Williams, B. P., et al. (2020). Mesospheric bore evolution and instability dynamics observed in PMC turbo imaging and rayleigh lidar profiling over northeastern Canada on 13 July 2018. *Journal of Geophysical Research: Atmospheres*, *125*, e2019JD032037. https://doi.org/10.1029/2019JD032037

Fritts, D. C., Wan, K., Werne, J., Lund, T., & Hecht, J. H. (2014). Modeling the implications of Kelvin-Helmholtz instability dynamics for airglow observations. *Journal of Geophysical Research: Atmospheres*, *119*, 8858–8871. https://doi.org/10.1002/2014JD021737

Fritts, D. C., Wang, L., Baumgarten, G., Miller, A. D., Geller, M. A., Jones, G., et al. (2017). High-resolution observations and modeling of turbulence sources, structures, and intensities in the upper mesosphere. *Journal of Atmospheric and Solar-Terrestrial Physics*, *162*, 57–78. Layered Phenomena in the Mesopause Region https://doi.org/10.1016/j.jastp.2016.11.006

Fritts, D. C., Wieland, S. A., Lund, T. S., Thorpe, S. A., & Hecht, J. H. (2020). Kelvin-Helmholtz billow interactions and instabilities in the mesosphere over the Andes Lidar Observatory: 2. Modeling and interpretation. *Journal of Geophysical Research: Atmospheres*, *125*, e2020JD033412. https://doi.org/10.1029/2020JD033412

Gardner, C. S. (2004). Performance capabilities of middle-atmosphere temperature lidars: Comparison of Na, Fe, K, Ca, Ca^+, and Rayleigh systems. *Applied Optics*, *43*(25), 4941–4956. https://doi.org/10.1364/AO.43.004941

Gardner, C. S., & Papen, G. C. (1995). Mesospheric na wind/temperature lidar. *The Review of Laser Engineering*, *23*(2), 131–134. https://doi.org/10.2184/lsj.23.131

Hecht, J. H. (2004). Instability layers and airglow imaging. *Reviews of Geophysics*, *42*(1), RG1001. https://doi.org/10.1029/2003RG000131

Hecht, J. H., Fritts, D. C., Wang, L., Gelinas, L. J., Rudy, R. J., Walterscheid, R. L., et al. (2018). Observations of the breakdown of mountain waves over the Andes Lidar Observatory at Cerro Pachon on 8/9 July 2012. *Journal of Geophysical Research: Atmospheres*, *123*, 276–299. https://doi.org/10.1002/2017JD027303

Hecht, J. H., Liu, A. Z., Walterscheid, R. L., & Rudy, R. J. (2005). Maui Mesosphere and Lower Thermosphere (Maui MALT) observations of the evolution of Kelvin-Helmholtz billows formed near 86 km altitude. *Journal of Geophysical Research*, *110*, D09S10. https://doi.org/10.1029/2003JD003908

Hecht, J. H., Wan, K., Gelinas, L. J., Fritts, D. C., Walterscheid, R. L., Rudy, R. J., et al. (2014). The life cycle of instability features measured from the Andes Lidar observatory over Cerro Pachon on 24 March 2012. *Journal of Geophysical Research: Atmospheres*, *119*, 8872–8898. https://doi.org/10.1002/2014JD021726

Hirt, C., Claessens, S., Fecher, T., Kuhn, M., Pail, R., & Rexer, M. (2013). New ultrahigh-resolution picture of Earth's gravity field. *Geophysical Research Letters*, *40*, 4279–4283. https://doi.org/10.1002/grl.50838

Hysell, D. L., Nossa, E., Larsen, M. F., Munro, J., Smith, S., Sulzer, M. P., & González, S. A. (2012). Dynamic instability in the lower thermosphere inferred from irregular sporadic *E* layers. *Journal of Geophysical Research*, *117*, A08305. https://doi.org/10.1029/2012JA017910

Kolmogorov, A. N., Levin, V., Hunt, J. C. R., Phillips, O. M., & Williams, D. (1991). The local structure of turbulence in incompressible viscous fluid for very large Reynolds numbers. *Proceedings of the Royal Society of London. Series A: Mathematical and Physical Sciences*, *434*(1890), 9–13. https://doi.org/10.1098/rspa.1991.0075

Larsen, M. F., Yamamoto, M., Fukao, S., Tsunoda, R. T., & Saito, A. (2005). Observations of neutral winds, wind shears, and wave structure during a sporadic-*E*/*QP* event. *Annales Geophysicae*, *23*(7), 2369–2375. https://doi.org/10.5194/angeo-23-2369-2005

Lehmacher, G. A., Guo, L., Kudeki, E., Reyes, P. M., Akgiray, A., & Chau, J. L. (2007). High-resolution observations of mesospheric layers with the Jicamarca VHF radar. *Advances in Space Research*, *40*(6), 734–743. https://doi.org/10.1016/j.asr.2007.05.059

Liu, A. Z., Hocking, W. K., Franke, S. J., & Thayaparan, T. (2002). Comparison of Na lidar and meteor radar wind measurements at Starfire Optical Range, NM, USA. *Journal of Atmospheric and Solar-Terrestrial Physics*, *64*(1), 31–40. https://doi.org/10.1016/S1364-6826(01)00095-5

Liu, A. Z., & Swenson, G. R. (2003). A modeling study of O_2 and OH airglow perturbations induced by atmospheric gravity waves. *Journal of Geophysical Research*, *108*(D4), 4151. https://doi.org/10.1029/2002JD002474

Mesquita, R. L. A., Larsen, M. F., Azeem, I., Stevens, M. H., Williams, B. P., Collins, R. L., & Li, J. (2020). In situ observations of neutral shear instability in the statically stable high-latitude mesosphere and lower thermosphere during quiet geomagnetic conditions. *Journal of Geophysical Research: Space Physics*, *125*, e2020JA027972. https://doi.org/10.1029/2020JA027972

Nappo, C. J. (2013). *An introduction to atmospheric gravity waves*. London: Academic Press.

Richardson, L. F., & Shaw, W. N. (1920). The supply of energy from and to atmospheric eddies. *Proceedings of the Royal Society of London. Series A, Containing Papers of a Mathematical and Physical Character*, *97*(686), 354–373. https://doi.org/10.1098/rspa.1920.0039

Roper, R. G., & Brosnahan, J. W. (1997). Imaging Doppler interferometry and the measurement of atmospheric turbulence. *Radio Science*, *32*(3), 1137–1148. https://doi.org/10.1029/97RS00089

Swenson, G. R., & Liu, A. Z. (1998). A model for calculating acoustic gravity wave energy and momentum flux in the mesosphere from OH airglow. *Geophysical Research Letters*, *25*(4), 477–480. https://doi.org/10.1029/98GL00132

Thorpe, S. A. (1985). Laboratory observations of secondary structures in Kelvin-Helmhoitz billows and consequences for ocean mixing. *Geophysical & Astrophysical Fluid Dynamics*, *34*(1–4), 175–199. https://doi.org/10.1080/03091928508245442

Thorpe, S. A. (1987). Transitional phenomena and the development of turbulence in stratified fluids: A review. *Journal of Geophysical Research*, *92*(C5), 5231–5248. https://doi.org/10.1029/JC092iC05p05231

Thorpe, S. A. (2002). The axial coherence of Kelvin-Helmholtz billows. *Quarterly Journal of the Royal Meteorological Society*, *128*(583), 1529–1542. https://doi.org/10.1002/qj.200212858307

Thorpe, S. A. (Ed.) (2005). *The turbulent ocean*. Cambridge, UK: Cambridge Univ. Press.

Walterscheid, R. L., Gelinas, L. J., Hecht, J. H., & Liu, A. Z. (2013). Instability structures during periods of large Richardson number ($ri > 1/4$): Evidence of parametric instability. *Journal of Geophysical Research: Atmospheres*, *118*, 6929–6939. https://doi.org/10.1002/jgrd.50514

Walterscheid, R. L., & Hickey, M. P. (2005). Acoustic waves generated by gusty flow over hilly terrain. *Journal of Geophysical Research*, *110*, A10307. https://doi.org/10.1029/2005JA011166

Walterscheid, R. L., Hickey, M. P., & Schubert, G. (2013). Wave heating and jeans escape in the Martian upper atmosphere. *Journal of Geophysical Research: Planets*, *118*, 2413–2422. https://doi.org/10.1002/jgre.20164

Weinstock, J. (1981). Energy dissipation rates of turbulence in the stable free atmosphere. *Journal of the Atmospheric Sciences*, *38*(4), 880–883. https://doi.org/10.1175/1520-0469(1981)038<0880:EDROTI>2.0.CO;2